Cathodic chloride extraction treatment of a late bronze-age artifact affected by bronze disease in room-temperature ionic-liquid 1-ethyl-3-methylimidazolium bis(trifluoromethanesulfonyl)imide (EMI-TFSI)

**Giuseppe Giovannelli · Lucia D'Urzo ·
Giovanna Maggiulli · Stefano Natali · Cosimo Pagliara ·
Ivonne Sgura · Benedetto Bozzini**

Abstract This paper concentrates on a novel approach to the electrochemical treatment of bronze disease, based on the use of room-temperature ionic liquids (RTIL). In particular, we employed 1-ethyl-3-methylimidazolium bis(trifluorome-thanesulfonyl)imide as the electrolyte for the galvanostatic cathodic treatment of a late bronze-age artifact that had been exposed to marine environment during its history, dating back to ca. 1100 B.C. After an accurate metallographic and structural analysis of the as-found object—proving, among other findings, that bronze disease is essentially related to the presence of nantokite locked inside subsurface pits of typical equivalent diameter of several hundred micrometers, we subjected it to optimal electrochemical conditions, showing—on the basis of X-ray diffraction—that nantokite could be effectively removed and Cu(I) reduced to metallic Cu. Numerical computations in the full three-dimensional pit geometry, with realistic nonlinear electrochemical boundary conditions, provide the theoretical framework for the choice of RTIL—as opposed to aqueous solutions—and for the quantitative evaluation of Cl⁻ removal rates.

G. Giovannelli · S. Natali
Dipartimento ICMMPM, Università di Roma "La Sapienza",
v. Eudossiana 18,
00185 Rome, Italy

L. D'Urzo · B. Bozzini (✉)
Brindisi Fuel Cell Durability Laboratory, Università del Salento,
S.S. 7 Brindisi-Taranto km 7+300,
72100 Brindisi, Italy
e-mail: benedetto.bozzini@unisalento.it

G. Maggiulli · C. Pagliara
Dipartimento di Beni Culturali, Università del Salento,
via D. Birago 64,
73100 Lecce, Italy

I. Sgura
Dipartimento di Matematica, Università del Salento,
via Arnesano,
73100 Lecce, Italy

List of the symbols and dimensions of model quantities

Latin letters

B_{an}^{Cu}	anodic Tafel slope of Cu electrodeposition reaction [V]
B_{cat}^{Cu}	cathodic Tafel slope Cu electrodeposition reaction [V]
B_{an}^{H}	anodic Tafel slope of HER [V]
B_{cat}^{H}	cathodic Tafel slope of HER [V]
C_i	concentration of species i [mol cm^{-3}]
D_i	diffusion coefficient of species i [cm^2 s^{-1}]
F	Faraday constant [C eq^{-1}]
i	current density applied during the galvanostatic experiment [C cm^{-2} s^{-1}]
i_o^{Cu}	exchange current density of Cu electrodeposition reaction [C cm^{-2} s^{-1}]
i_o^{H}	exchange current density of HER [C cm^{-2} s^{-1}]
k_o^{Cu}	cathodic kinetic constant of Cu electrodeposition reaction [C cm mol^{-1} s^{-1}]
$\vec{n}$	unit vector normal to a given surface [1]
R	gas constant [C V K^{-1} mol^{-1}]
t	time [s]
T	absolute temperature [K]
z_i	valence of ion i [eq mol^{-1}]

Greek letters

κ_{aq}	electrical conductivity of the aqueous solution [C V^{-1} s^{-1} cm^{-1}]

κ_{IL}	electrical conductivity of the RTIL [C V^{-1} s^{-1} cm^{-1}]
Φ	potential [V]
Φ_o^{Cl}	equilibrium potential of the Cl$_2$ evolution reaction [V]
Φ_o^{Cu}	equilibrium potential of Cu electrodeposition reaction [V]
Φ_o^{H}	equilibrium potential of HER [V]
Φ_o^{O}	equilibrium potential of OER [V]

Other symbols

$\bullet$	scalar product
$\overrightarrow{\nabla}$	gradient operator, vectorial [cm^{-1}]
$\nabla_n \triangleq \overrightarrow{n} \bullet \overrightarrow{\nabla}$	normal gradient operator, scalar [cm^{-1}]
$\overrightarrow{\nabla} \bullet$	divergence operator, vectorial [cm^{-1}]
$\nabla^2 \triangleq \overrightarrow{\nabla} \bullet \overrightarrow{\nabla}$	Laplacian operator, scalar [cm^{-2}]
$\partial/\partial t$	partial time derivative operator [s^{-1}]

List of the numerical values of model constants

$B_{an}^{Cu} = B_{cat}^{Cu}$	0.052 V
$B_{an}^{H} = B_{cat}^{H}$	0.046 V
$D_1 = D_2 = 10^{-5}$ cm^2 s^{-1}	in both water and RTIL (where $D_1 = D_{Cl}$ and $D_2 = D_{Cu}$)
F	96,500 C eq^{-1}
i_o^{Cu}	2.4×10^{-3} C·cm^{-2}·s^{-1}
i_o^{H}	8.1×10^{-7} C cm^{-2}·s^{-1}
k_o^{Cu}	0.067 C cm mol^{-1} s^{-1}
R	8.31 C V K^{-1} mol^{-1}
T	300 K
z_1	−1 (where $z_1 = z_{Cl}$)
z_2	+1 (where $z_2 = z_{Cu}$)
κ_{aq}	0.1 C V^{-1} s^{-1} cm^{-1}
κ_{IL}	0.01 C V^{-1} s^{-1} cm^{-1}
Φ_o^{Cl}	1.36 V$_{SHE}$
Φ_o^{Cu}	0.137 V$_{SHE}$
Φ_o^{H}	-0.414 V$_{SHE}$
Φ_o^{O}	0.815 V$_{SHE}$
n.b.	The issue regarding use of RE in RTIL is currently still open. For the present purpose, we assume that the SHE can be regarded as an acceptable scale also for RTILs, even though the relevant thermodynamics does not apply, of course.

Introduction

The last 20 years have seen an increasing interest [1, 2] for a multidisciplinary scientific approach to historical metallurgy, covering a variety of research fields: (1) mining processes and manufacturing technology; (2) history of cultural, social, and economic backgrounds; (3) conservation and preservation science. As far as conservation science is concerned, the emphasis has moved from restoring an object as closely as possible to its original state to using it as a primary research document in order to learn as much as possible about its historical context, technology, use, and environment.

This work focuses on a bronze artifact which has been found in its original position, corresponding to a late bronze-age (1200–1000 B.C.) occupation stratum in a hoard of bronze objects in the archeological site of Roca (Lecce, Italy). Field work in this area, which started as early as 1980 under the direction of the Dipartimento di Beni Culturali dell'Università di Lecce, unveiled—through successive excavation campaigns—the remnants of buildings and material culture relics attesting human occupation from the medium bronze age (1800–1600 B.C.) to the late medieval period (A.D. 1400–1500).

The site of Roca [3, 4] constitutes a "unicum" of protohistoric archeology in peninsular Italy, as far as the level of the manufacture and number and extent of the findings are concerned. All the objects found in the Roca site constitute a tight-knit group of artifacts, both in terms of chronology and cultural belonging, since they result from a single historical context that can be subjected to systematic interdisciplinary investigations.

The hoard [5] was deposited inside a ceramic pot (truncated-cone jar), encased in the rock up to the edge, closed by a square and flat stone and covered with a mortar of tuff-dust. It is comprised uniquely of bronze scraps, ascribable mostly to sickles, axes, bun, and plano-convex ingots and few fragments of buttons, foils, and bars. All the hoard objects have been found in a good state of preservation. The most represented category is that of the axes: shaft-hole axes, winged axes, and especially socketed axes; the last type is often decorated on the stem ("hourglass," triangular, or vertical).

A preliminary archeometallurgical characterization revealed marked differences among these artifacts as far as the crystal structure of the corrosion patina and the elemental composition of the sound metal remnants are concerned. While a comprehensive archeological interpretation of these artifacts is still lacking (foundry hoard or traders' hoard), still, the single-alloy content of this hoard strongly hints at the existence of a productive chain in bronze metallurgy, based at the excavated site.

Some of the hoard objects exhibit clear symptoms of "bronze disease" [6] and need urgent and specific preservation actions. Bronze disease [7, 8] may be defined as the process of interaction of CuCl within the bronze patina with moisture and air, resulting in corrosion of the underlying alloy. The products of the reaction are light-green powdery basic Cu(II) chlorides. The overall damaging reaction

seems to exhibit autocatalytic behavior and to be photo-enhanced. The conservation of corroded copper alloys and the stabilization of active bronze disease are two of the most difficult problems facing the archeological conservator archeologists. According to the traditionally accepted reaction scheme of [6], the principal reaction mechanism is the production of cuprite by hydrolysis of CuCl. This reaction is believed to be inactive in burial conditions [7]. The hydrochloric acid generated by this reaction can, in turn, attack Cu, thus producing fresh CuCl and hydrogen. This model at the moment can only be regarded as a guideline for further refinement: much more insightful investigations on the fundamental corrosion and materials science aspects are needed for a fully operative knowledge of this topic. Currently, we know that the formation of crystalline CuCl has been disclosed in the pitting corrosion of copper [9, 10] and that the cuprite that forms over the CuCl layer acts as a diffusion barrier and as a bipolar electrode with the anodic reaction going on in the inner surface of the cuprite layer and the cathodic one on the outer surface. Cuprous ions diffuse through the cuprite and can be oxidized by the oxygen dissolved in the electrolyte. A fraction of these ions can be precipitated as basic salts and another one can be reduced back to Cu(I) at the outer surface of the membrane. The anodic reaction within the pit gives rise to an increase of Cu(II) concentration. From a thermodynamic point of view, the examination of the Pourbaix diagram [11] suggests that at the pH typical for bronze disease pits (pH approximately 3 to 5) copper cuprite and nantokite are stable at approximately 300 mV NHE. Infrared spectroscopy has been employed for the identification of bronze corrosion products [12]. An electrochemical study on the formation of basic copper chlorides as a Cu patination product in marine environment has been published [13]. Some simulation experiments have been reported on the reactions of CuCl in contact with copper and water: copper trihydroxychloride has been shown to form rather than cuprite [14]. The importance of mass-transport processes in the formation of chloride-containing patinae [15] has been highlighted as well.

The first serious attempt to find a method for restoring badly corroded ancient bronzes appeared in 1923 [16]. The method involved an electrolytic bath with the object as cathode contained in a cell filled with a solution of sodium hydroxide. The authors claimed that details were revealed, there was no pitting, and completely corroded sections of the objects were reduced back to metal. The principle of this treatment is very simple: a direct current is applied between the bronze object and an anode placed externally. The electric scheme is the same as that of the well-known cathodic protection. Two different methods are in use, respectively, based on: (1) galvanic coupling of the metal to be treated with a less noble metal and (2) an impressed current by means of a current feeder. The positive effects of current circulation are mainly concerned with the removal of the chlorides from the patina and the deposition of copper at the cathode. The quantity of chloride removed depends on the total charge as well as on the efficiency of the process. Of course, only a fraction of the total current is effective in removing chloride ions, corresponding to the chloride ion transport number in the relevant electrolyte. Predictions of chloride removal can be made using physicochemical models and estimated transport numbers. Modeling of current distribution and monitoring of the progress of the reaction are necessary. Although direct references were not found in literature, a list of papers and books concerning the same electrochemical treatment for different cases are available [17–19]. These techniques (often in combination with selective mechanical removal of incrustations) were extensively employed since the 1930s through the 1950s in the US and in Germany [20]; some bronzes subjected to these treatments developed after some years blue–green excrescences, even in zones that did not correspond to formerly active areas [21].

A change in attitude towards stabilizing severely corroded or actively corroding bronzes can be recorded in the early 1960s; since then on, a number of chemical and electrochemical treatments have been published in the conservation literature with the goal of stabilizing the bronze artifact while preserving its patina. Chemical methods for stabilization, involving the use of sodium sesquicarbonate, were introduced in 1963 [6]. The hydroxyl ions of the sodium sesquicarbonate react chemically with the insoluble CuCl at the bronze surface, forming cuprite and neutralizing HCl and any acid by-product formed by hydrolysis, to produce soluble sodium chloride. The removal of the chloride ions is completed with a continuous change of the solution. The method is simple, effective, and inexpensive; however, soaking can take over a year to complete, and it was demonstrated that, although the sodium sesquicarbonate dissolved the chlorides, it also dissolved some metallic copper [22]. The use of benzotriazole (BTA) was recommended in 1967 for the treatment of bronze disease without removing the patina [23] and this treatment quickly became the favored method owing to its simplicity. BTA is a well-known corrosion inhibitor for pure copper metal or copper alloys, widely used over the past 40 years. Treatment with BTA does not remove the cuprous chloride from the artifact; rather, it forms a barrier between CuCl and the atmosphere. Unfortunately, (1) BTA is a suspect carcinogen and its use is subjected to uncomfortable precautions and (2) tests carried out by the British Museum [24] indicate that, if active bronze disease is present, attempts to stabilize the object with BTA tend to fail due to the unceasing formation of CuCl in the corrosion layers.

As a matter of fact, the notable compositional inhomogeneity of archeological bronzes and the heterogeneity of the corrosion products can hamper a precise comparison

between test results. As a consequence, the resulting data are typically specific to the individual artifact and its history and conditions and poorly representative of a general behavior. In many instances, the inhibitor has to be applied immediately after excavation, since field laboratories are not generally equipped with air-extraction systems. The development of innovative corrosion inhibitors is not a simple approach because of the scatter of patina and bronze chemistries and of the difficulty in performing representative screening tests with nonarcheological materials. In any case, the type of inhibiting action should be based on a peculiar type of complex formation, resulting in a polymeric layer. In the ideal case, the inhibitor (1) should adsorb or chemically bond to the substrate, (2) should be able to penetrate inside the pit in pitting corrosion, (3) should not modify the visual appearance of the patina, and (4) should not be hazardous or harmful to the user.

An alternative approach would be to apply a fast and reliable electrochemical method without the addition of extraneous materials to the artifact. In this paper, we propose a variant of the traditional galvanostatic cathodic treatment, employing a hydrophobic room-temperature ionic liquid (RTIL). The rationale of using an accurately deaerated, hydrophobic RTIL instead of the traditional—and largely unsatisfactory—aqueous solutions for galvanostatic cathodic chloride extraction is that the absence of any electrolyte reaction in a wide potential window would allow efficient electric field penetration into the subsurface pits and cracks containing harmful CuCl. In aqueous solutions, instead, water decomposition on the outer surface of the artifact is expected to give rise to electric field screening of the subsurface defects that are most in need of being cathodically treated.

Experimental

The investigated artifact

The object of the present investigation is the metal fragment, of maximum dimensions $75 \times 25 \times 3$ mm^3, from the aforementioned hoard, pertaining to socketed axes, depicted in Fig. 1 in the as-found state. This artifact is heavily encrusted (Fig. 2) with an external altered zone exhibiting green and blue patinae as well as mineral species.

Morphological characterization

The object was sampled by removing an apical fragment, weighing approximately 80 mg, with a diamond saw. Neither grinding nor polishing treatments were performed in the cross-sectional plane of the sampled fragment in order to prevent edge-rounding and loss of loose patina

Fig. 1 The investigated metal fragment from the Roca Hoard (late bronze age, 1200–1000 B.C.)

fragments. Light microscopy observations were carried out with a Leitz Laborlux 12 ME S attached to a Nikon Coolpix 3500. In-plane and cross-sectional scanning electron microscopy (SEM) was performed with a HITACHI S 2500 SEM equipped with an LaB$_6$ electron source and a scintillation electron photodetector. The typical working pressure was 10^{-7} mbar. A mild etching with alcoholic FeCl$_3$ was applied before SEM examination.

Structural characterization

The structural characterization of the surface phases was performed by X-ray diffraction (XRD) on a plane portion of the object, measuring approximately 5×5 mm^2. The identification of the subsurface species was obtained by sequentially removing [25] thin layers (about 20 µm) of the patina material by surface grinding on a 1,200-mesh

Fig. 2 Detail of the crust covering the object depicted in Fig. 1

grinding paper and taking XRD measurements after each successive grinding stage. XRD measurements were made with a Philips PW 1830 diffractometer equipped with a Philips X-PERT vertical Bragg–Brentano powder goniometer. A step–scan mode was used in the 2θ range from $10°$ to $80°$ with a step width of $0.02°$ and a counting time of 5 s per step. The employed radiation was monochromated Cu Kα. The calculation of theoretical diffractograms and the generation of structure models were performed using the PowderCell software [26].

Elemental analysis by EDX

Quantitative compositional analysis of the fragment was performed by energy dispersive X-ray spectroscopy (EDX) in the same vacuum chamber and with the same electron source as the SEM, using a Li-doped Si detector. Compositional data of the relevant item have also been collected by means a portable ED-XRF spectrometer (Spectro X-test, lateral resolution of 1×1 mm^2, penetration range about 10 μm), equipped with a Cu anode and a light-element detector. This comparatively good lateral resolution [27] is suitable for the compositional mapping of heterogeneous alloys.

Electrochemical measurements

Galvanostatic and potentiodynamic measurements were carried out with an AMEL 5000 potentiostat. The electrolyte was pure 1-ethyl-3-methylimidazolium bis(trifluoromethanesulfonyl)imide (EMI-TFSI) from IoliTec. This is a highly hydrophobic RTIL with a large electrochemical window (approximately $-3\div+3$ V vs. Au quasi-reference electrode [QRE]). Since the oxygen solubility in EMI-TFSI is essentially the same as in water, in order to profit of the properties of this electrolyte, accurate deaeration is required. In our experiments, EMI-TFSI has been accurately (at least 1 h before electrochemical treatment) and continuously degassed with Ar. For this reason, rather noisy electrochemical measurements were obtained, though without significant impact on the meaning on the results. A three-electrode configuration was used. The pieces to be treated were held in a hanging-meniscus configuration, so that only the patina contacted the EMI-TFSI surface. The counter-electrode was a large-area (10 cm^2) graphite slab, lying parallel to the RTIL free surface. The QRE was a Au wire, annealed in a butane flame; all potentials are reported vs. Au QRE. The QRE tip was located behind the hanging working electrode. As one can conclude from many references in the literature on electrochemistry in RTILs and from the extensive relevant discussion contained in [28, pp. 296–307], the use of QREs is state-of-the-art in the relevant field.

Numerical computations

The three-dimensional (3D) compositional and current density distributions have been computed by the COMSOL Multiphysics solver, based on the finite-element method. The robustness of the computational results with respect to meshing and the choice of the linear integrator have been cross-checked with state-of-the-art numerical procedures and adaptive grid techniques [29].

Results and discussion

Structural and chemical analysis of the as-found object

EDX, optical light microscopy, and cross-sectional SEM

EDX analyses on large regions (0.5×0.5 mm^2) of the unetched sample *surface* yield a Sn content of 13.1 ± 0.4 w/o, any other alloying element was below the detection limit (approximately 0.2 w/o). The average Sn content of metallographic *cross-sections* resulted to be 13.3 w/o; again, no other alloying metal could be detected. We also estimated the Sn content by the Végard method, based on XRD data [30]; of course, this approach is far less sensitive to surface dealloying and local compositional variations. In the case at hand, the Végard relation can be written as: $a_\alpha=a_{Cu}+1.054C_{Sn}$. Where a_α is the cell constant of the alloy, a_{Cu} that of pure Cu and C_{Sn} is the Sn concentration, expressed as w/o. The measured cell constant value a_α resulted to be 3.6963 ± 0.0002 Å, yielding a Sn content of 13.49 w/o.

The observed Sn content corresponds to a "low-tin" bronze, according to classical denomination [31]. Accordingly, the light microscopy image shown in Fig. 3 shows the dendritic cast microstructure, which is typical for bronze alloys of this composition, that have not undergone hammering-and-annealing treatments. This particular low-tin bronze alloy is extensively segregated with cored dendritic growth and an infill of the $\alpha + \delta$ phases surrounding the dendritic arms. For historical metal alloys of this composition, the precipitation of a secondary α phase is generally expected [32]. Such a behavior is not observed in this particular case, possibly because of a slow cooling process. A closer observation of Fig. 3 reveals the prevailing type of corrosion that is observed in this object. In the partially corroded area on the right side, the darker regions correspond to corroded δ phase and the neighboring bright metal regions correspond to the intact Cu-rich α phase. This preferential corrosion of the Sn-rich phase in Cu–Sn alloys is commonly referred to as "type I corrosion" [33] and it is generally associated with the presence of chloride ions.
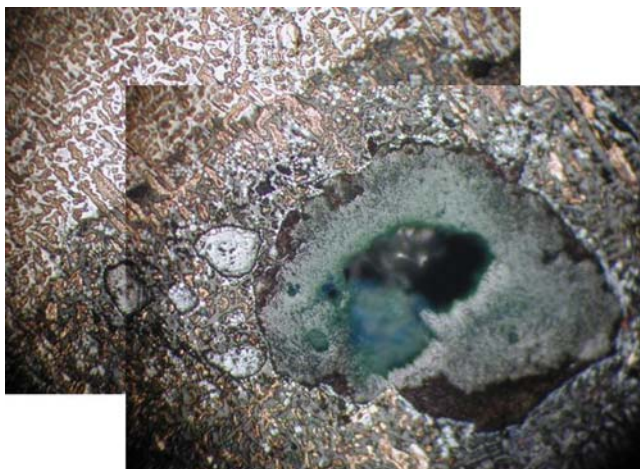
Fig. 3 Light microscopy image of a cross-section of the object shown in Fig. 2

The same area was observed by SEM with backscattered electrons (Fig. 4). In both Figs. 3 and 4, the corroded areas exhibit an elemental composition corresponding to Cu_2O. Sparse globular copper sulfides of compositions Cu_xS with x in the range 0.9–1.0 can be detected in the SEM image: sulfide attack on the α phase has been reported in [34]. Details of the EDX elemental distribution of O, S, Cu, and Sn in different locations of the area shown in Figs. 3 and 4 are shown in Fig. 5. In particular, the S distribution reveals that the sulfide attack on the α phase is accompanied by the diffusion of Sn-containing species, eventually resulting in the formation of cassiterite, as proved by XRD analysis in Section 3.1.2.

Structure of the corrosion patina

Figure 6 reports the X-ray diffractograms obtained by successively removing different thicknesses of patina, as indicated in Section 2.3. It is thus possible to evaluate the relative abundances of the patina constituents, as a function of depth. The green-bluish outer layer results to be mainly composed of the secondary oxidation products connellite $Cu_{19}Cl_4(SO_4)(OH)_{32}\cdot3(H_2O)$ and malachite $Cu_2(CO_3)(OH)_2$ and the two isomorphous compounds atacamite and paratacamite $Cu_2Cl(OH)_3$, together with minor amounts of calcite resulting from soil encrustation. It is worth noting that connellite is a rare secondary corrosion product of copper alloys that typically forms upon exposing bronze objects to solutions containing sulfate and chloride ions [35]. Increasing depth, two successive layers containing, respectively, cuprite and nantokite, are found. The inner part of the patina contains poorly crystallized cassiterite [36], along with some chalcocite. The diffractogram corresponding to a depth of 180 μm in Fig. 6 corresponds to the intact metallic remnant and enabled us to assign the exact crystal structure of the metal alloy.

The cross-sectional secondary-electron SEM image shown in Fig. 7 depicts the corrosion structure described in this section. In particular, one can notice the successive layers forming the corrosion patina onto unaltered bonze: (0) secondary corrosion products; (1) cuprite layer; (2) cubic crystals of nantokite; (3) partially crystallized cassiterite; (4) uncorroded α phase.

Theoretical description of the electrochemical process and numerical computations

Model equations

In the present case, cognate to that of electrochemical Cl^--extraction processes used in concrete treatment (for a recent, comprehensive review, see [37]), a classical mass-transport model can be adopted (e.g., [38]) with the approximation of identifying activities with concentrations. A simplified view of the chemistry of the relevant system is that the chemical species of interest that are present are just CuCl and the electrolyte. The electrolyte is either neutral water, made conductive with some inert salt, or an RTIL. Assuming that the electrolytes are not oxygenated, we can state that water is electroactive, owing to OER and HER, while the RTIL is electrochemically inert within its large electrochemical window. The concentrations of Cl^- (denoted by C_1 in the following) and Cu^+ (indicated as C_2) are affected by the electrochemical treatment, but the concentration of water can be assumed not to vary locally. Fast migration and diffusion of OH^- produced in the reduction of water can be assumed to rapidly homogenize the pH and the presence of a large water reservoir allows
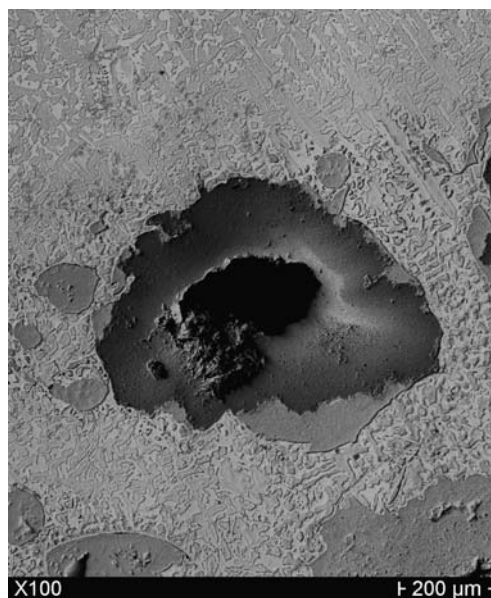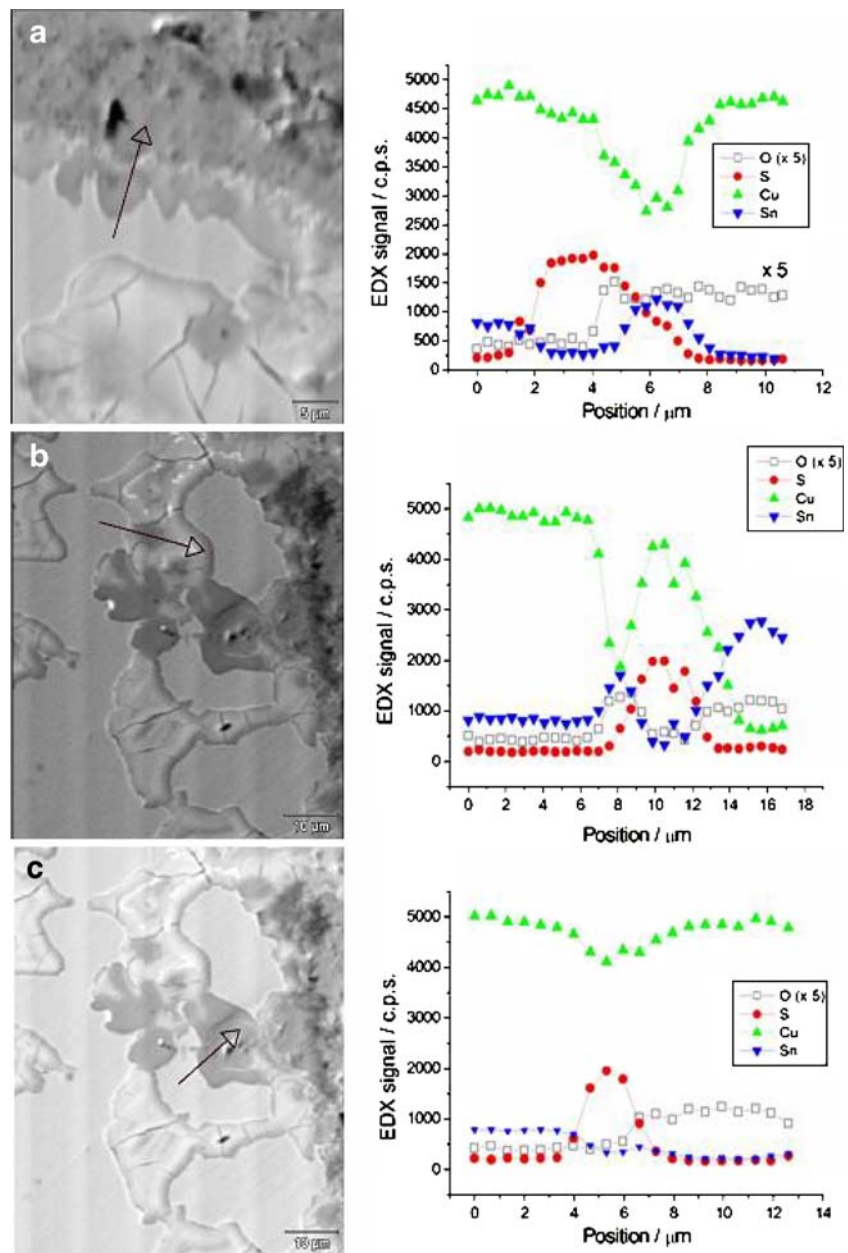

Fig. 4 Secondary-electron SEM image of the region shown in Fig. 3

Fig. 5 EDX line profiles for O, S, Cu, and Sn in the indicated locations of the area depicted in Figs. 3 and 4


the assumption that the pH is constant and fixed to 7. Under these assumptions, we need to write mass-balance equations only for C_1 and C_2. We can thus write the model equations as:

The reactivity of water will thus be accounted for only via the boundary conditions (BC).

The integration domain as well as the boundary and initial conditions depend on the details of the process and

$$\begin{cases} \dfrac{\partial C_1}{\partial t} = D_1 \cdot \nabla^2 C_1 + D_1 \cdot \dfrac{z_1 F}{RT} \cdot \vec{\nabla} \bullet \left(C_1 \cdot \vec{\nabla}\Phi \right) & (1) \\[2ex] \dfrac{\partial C_2}{\partial t} = D_2 \cdot \nabla^2 C_2 + D_2 \cdot \dfrac{z_2 F}{RT} \cdot \vec{\nabla} \bullet \left(C_2 \cdot \vec{\nabla}\Phi \right) & (2) \\[2ex] \nabla^2 \Phi = 0 & (3) \end{cases}$$

Fig. 6 X-ray diffractograms obtained by removing the indicated thicknesses of patina from the as-found object
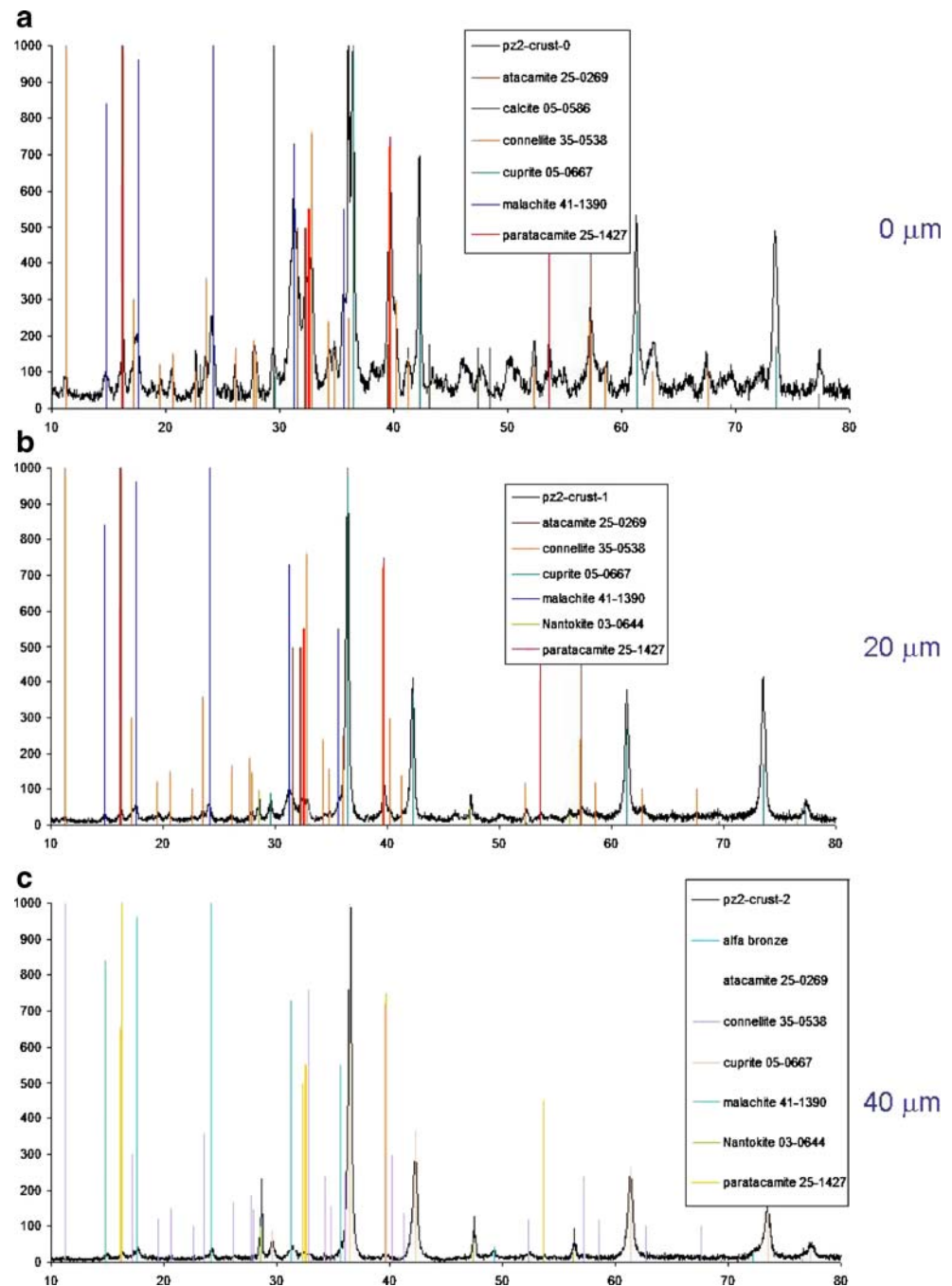
are discussed below. The time dependence of $\Phi(x,y,z,t)$ is accounted for via the coupling with C_1 and C_2, under the condition that its curvature is constant, as per Eq. 4.

In principle, the fact that the Cu^+ reduction reaction leads to the formation of a metallic Cu layer can give rise to variations in domain geometry. On the basis of simple stoichiometric considerations, it can be shown that the case of quantitative, homogeneous reduction of the amount of CuCl that can be incorporated in a typical pore would give rise to the deposition of approximately 25 μm of Cu, a thickness that does not justify the adoption of a moving-boundary approach.

The dimensions and numerical values of the quantities appearing in this equation and in all the following ones are listed at the beginning of this document.

Domain of integration

From metallographic evidence reported in Section 3.1 the domain where Eq. 4 has to be integrated can be schematized as depicted in Fig. 8: a subsurface pit—filled with CuCl—is connected with the external electrolyte through a crack, typically a grain–boundary decohesion.

Fig. 6 (continued)
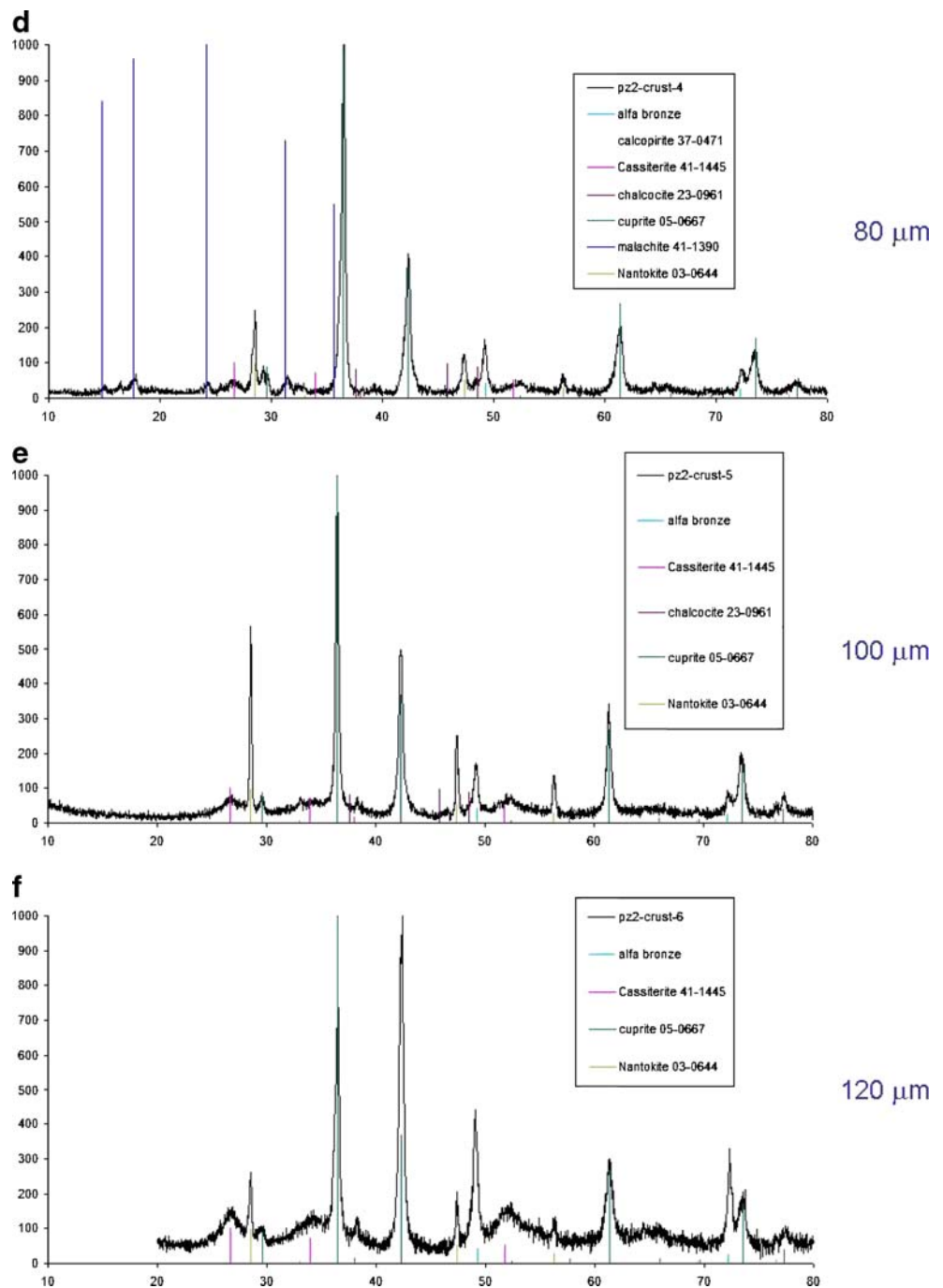
The crack is filled with CuCl and the external electrolyte is either an aqueous solution or an RTIL.

Boundary and initial conditions

The difference between the aqueous solution and the RTIL is taken into account through the BCs. In order to discuss this difference, we refer to Fig. 9. This figure exhibits two types of BCs corresponding to the piece to be treated, drawn in blue and green, respectively. The surface (green) BC corresponds to the external part of the piece, facing the free electrolyte; the internal (blue) BCs represent the internal surface of the pit.

Surface BC for the aqueous solution In the case of a deaerated aqueous solution, the surface (green) BC can act as a cathodic BC, corresponding to the water-reduction reaction that can be described approximately as:
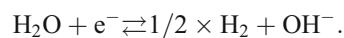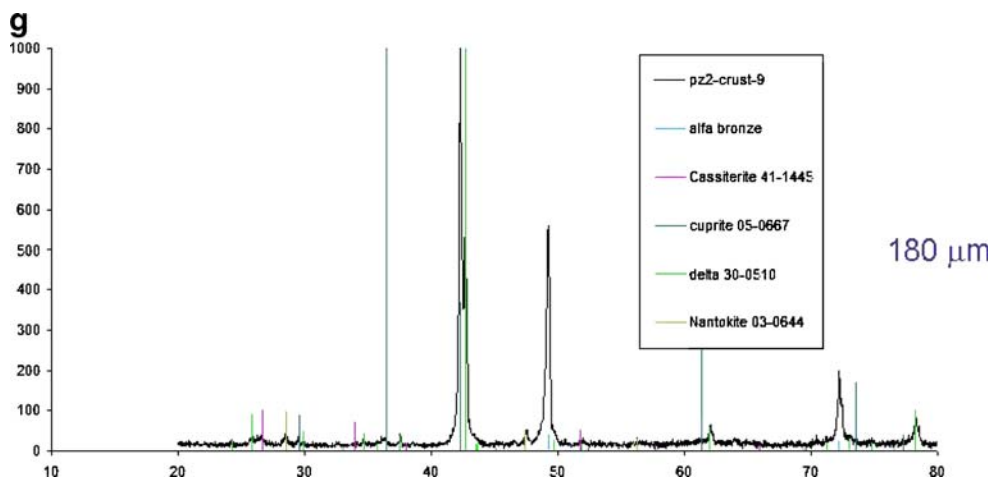
$$H_2O + e^- \rightleftarrows 1/2 \times H_2 + OH^-.$$

Fig. 6 (continued)

The cathodic kinetics of this reaction can be described as:

$$i = i_o^H \times \left(\exp\left[\frac{\Phi - \Phi_o^H}{B_{an}^H}\right] - \exp\left[-\frac{\Phi - \Phi_o^H}{B_{cat}^H}\right] \right) \tag{4}$$

where i_o^H is the exchange current density, B_{an}^H is the anodic Tafel slope, and B_{cat}^H is the cathodic Tafel slope. The numerical values of the constants reported in the list at the beginning of this document incorporate literature data for a Cu cathode in a neutral solution ([39] p. 43).

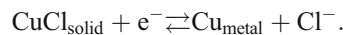Therefore, in this case, the BCs are:
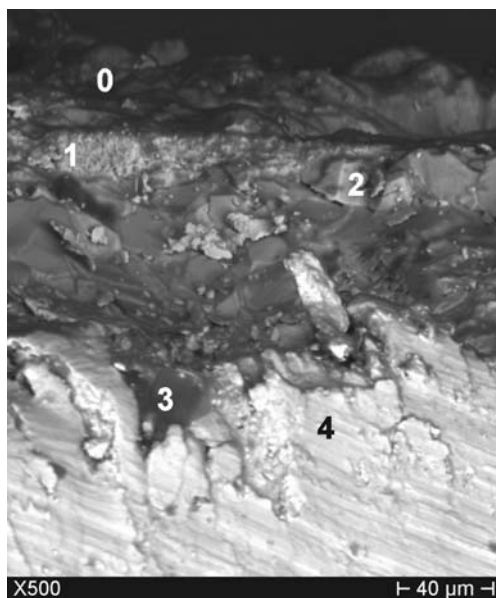
$$J_n(C_1) = 0 \tag{5}$$

Fig. 7 Secondary-electron SEM micrograph of the patina cross-section showing *0* secondary corrosion products, *1* cuprite layer, *2* cubic crystals of nantokite, *3* partially crystallized cassiterite, *4* uncorroded α phase

$$J_n(C_2) = 0 \tag{6}$$

$$\nabla_n \Phi = \frac{i_o^H}{\kappa_{aq}} \times \left(\exp\left[\frac{\Phi - \Phi_o^H}{B_{an}^H}\right] - \exp\left[-\frac{\Phi - \Phi_o^H}{B_{cat}^H}\right] \right) \tag{7}$$

where $J_n(C_i)$ is the normal flux of species i and κ_{aq} is the conductivity of the aqueous solution.

Surface BC for RTIL In the case of a deaerated RTIL—that does not exhibit any electrochemical reactivity over an extended potential region—the surface BC is simply an insulating one, which can be treated as detailed below in "Insulating BCs".

Cathodic internal BCs Both in the aqueous solution and in RTIL, the internal (blue) border is the location where a cathodic reaction takes place. In both cases, the cathodic reaction can be taken to be the reduction of Cu(I) present in the CuCl precipitate locked in the pits. With RTIL, this is the only cathodic reaction going on in the whole system, while in the aqueous solution, the HER can also occur at the surface BC (i.e. green border, see "Surface BC for the aqueous solution"). In the absence of quantitative information regarding the kinetics of these processes in RTIL, we can assume that the reduction mechanism is the same in both systems and use—in our first-approximation approach—the same kinetic constants. A reaction mechanism proposed by [40], which we can take on for our model, is:

$$CuCl_{solid} + e^- \rightleftarrows Cu_{metal} + Cl^-.$$

This reactivity scenario would correspond, in both systems (with the only difference of the conductivities κ_{aq} and κ_{IL}), to the following BCs:

$$J_n(C_1) = 0 \tag{8}$$

Fig. 8 Integration domain for the model equations. *1* Schematic view of the composition of the subdomains (*A* is either water of RTIL, *B* is CuCl). *2* The actual 3D domain implemented for COMSOL computations
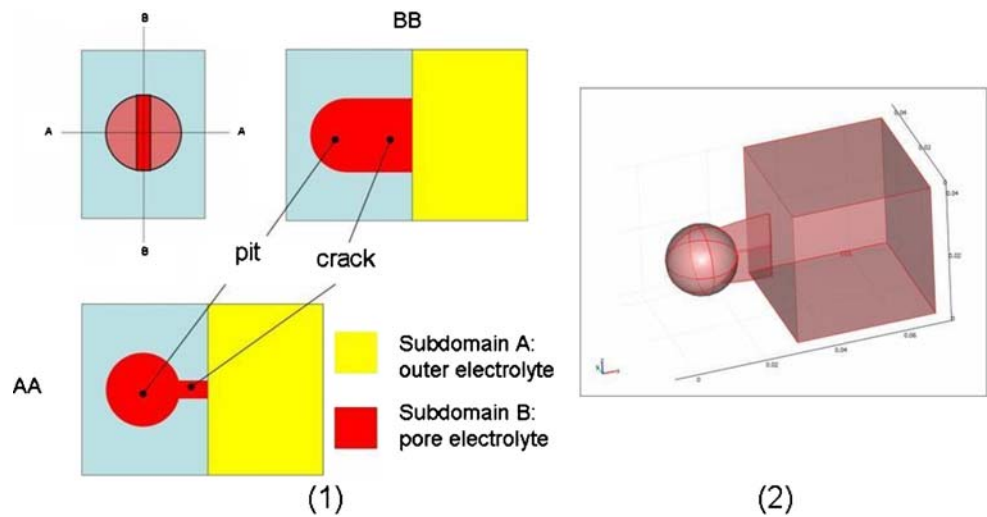
$$\nabla_n C_2 = \frac{\kappa_{aq,IL}}{z_2 F D_2} \times \nabla_n \Phi \tag{9}$$

$$\nabla_n \Phi = \frac{1}{\kappa_{aq,IL}}$$
$$\times \left(i_o^{Cu} \times \exp\left[\frac{\Phi - \Phi_o^{Cu}}{B_{an}^{Cu}}\right] - k_o^{Cu} \times C_2 \times \exp\left[-\frac{\Phi - \Phi_o^{Cu}}{B_{cat}^{Cu}}\right] \right). \tag{10}$$

The numerical values of the kinetic constants have been derived from [41, p. 475], reporting data on phenomenological electrodeposition kinetics from a chloride solution with the reduction of Cu(I) to Cu(0) being the rate-determining step.
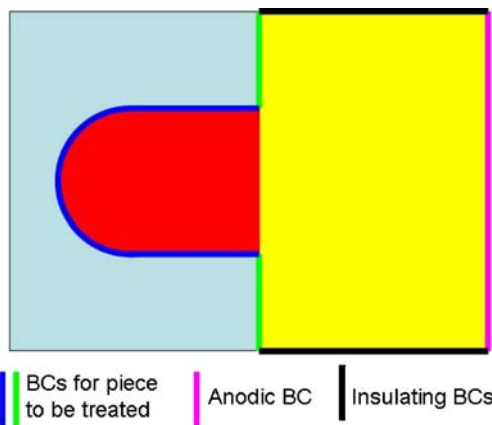

Fig. 9 Types of BC for the solution of the model equations. Two types of BCs correspond to the piece to be treated, drawn in *blue* and *green*, respectively. The surface BC (*green*) corresponds to the external part of the piece, facing the free electrolyte; the internal BC (*blue*) represents the surface of the pit. The other BCs are indicated on the drawing

Insulating BCs The black borders of Fig. 9, as well as the green ones when using the RTIL, correspond to insulating BCs that can be written as:

$$J_n(C_1) = 0 \tag{11}$$

$$J_n(C_2) = 0 \tag{12}$$

$$\nabla_n \Phi = 0. \tag{13}$$

Anodic BCs On the purple border of Fig. 9 we set formally anodic BCs with the following electrochemical meaning. In the real situation, the anode is typically located a few centimeters from the piece to be treated. This implies that the location of the purple border in Fig. 9 does not correspond to the actual anode location, but rather bounds a volume element close to the cathode and whose dimensions are of the same order of magnitude as those of the pit (approximately 1 mm). Of course, it would be possible to model the exact anode location, e.g., with special geometrical normalizations (see [42]), but this does not look necessary in the present situation. Furthermore, since the anodic BCs are located far enough from the pit/crack system, it can be assumed that the current density lines are homogeneously distributed over the anode itself.

Anodic BCs in aqueous solution In an aqueous solution, in the real situation, Cl^- ions flow from the cathode to the anode, but they typically do not react at the anode where the chief reaction is the OER:

$$H_2O \rightleftharpoons 1/2 \times O_2 + 2e^-.$$
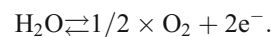
In fact, the standard equilibrium potentials in neutral solutions for Cl^- and OER are 1.36 and 0.815 V_{SHE},

respectively. As a first approximation, we can assume that the transport number of Cl^- is unitary. In the present model, we can thus numerically equate the expression of the flow of Cl^- through the purple border and the OER rate occurring at the anode.

The following BCs can thus be written:

$$\nabla_n C_1 = \frac{\kappa_{aq}}{z_1 F D_1} \times \nabla_n \Phi \qquad (14)$$

$$J_n(C_2) = 0 \qquad (15)$$

$$\nabla_n \Phi = \frac{i}{\kappa_{aq}}. \qquad (16)$$

Anodic BCs in RTIL In the case of RTIL, Cl^- ions are the only species that can be oxidized at the anode. Therefore, the BCs at the purple border can be assimilated to the electrochemical reaction rate of Cl^-, if the anode does not undergo oxidation. To the best of the authors' knowledge, no quantitative data is available either on Cl_2 evolution from RTILs or on the anodic behavior of electrodes in the relevant RTIL. Nevertheless, these uncertainties are expected to have a very limited bearing on the present study. In order to carry out our computations, we assume that the anode does not corrode and that the phenomenological Cl_2 evolution kinetics can be approximately taken to be the same as in aqueous solution. We thus write the BCs as:

$$\nabla_n C_1 = \frac{\kappa_{IL}}{z_1 F D_1} \times \nabla_n \Phi \qquad (17)$$

$$J_n(C_2) = 0 \qquad (18)$$

$$\nabla_n \Phi = \frac{i}{\kappa_{IL}}. \qquad (19)$$

Boundary between the pore (red) domain and external electrolyte (yellow) domain Flux continuity is imposed at this boundary for $\vec{\nabla} C_1$, $\vec{\nabla} C_2$, and $\vec{\nabla} \Phi$ describing the fact that (1) Cl^- flows out of the pore domain into the electrolyte domain, following the concentration gradient and the electric field; (2) Cu^+ in principle can flow out of the pore domain, under concentration gradient, but eventually will flow back into the pore, driven by the electric field; and (3) the electric field is continuous.

Initial conditions The initial conditions for $C_1(x,y,z,t=0)$ and $C_2(x,y,z,t=0)$ describe the fact that—before the electrochemical treatment—the pit and the crack connecting it to the outer electrolyte are filled with solid CuCl and no CuCl is present in the outer electrolyte.

Therefore, in the pore (red) domain of Fig. 8:

$$C_1(x,y,z,t=0) = C_2(x,y,z,t=0) = 0.036 \, mol \, cm^3 \qquad (20)$$

and in the free electrolyte (yellow) domain of Fig. 8:

$$C_1(x,y,z,t=0) = C_2(x,y,z,t=0) = 0 \qquad (21)$$

The concentration $0.036 \, mol \, cm^{-3}$ corresponds to that of the solid CuCl precipitate. As far as the ICs for Φ are concerned, the anodic boundary discussed in "Anodic BCs in RTIL" in fact represents a location within the electrolyte where the reference electrode is placed. This location can
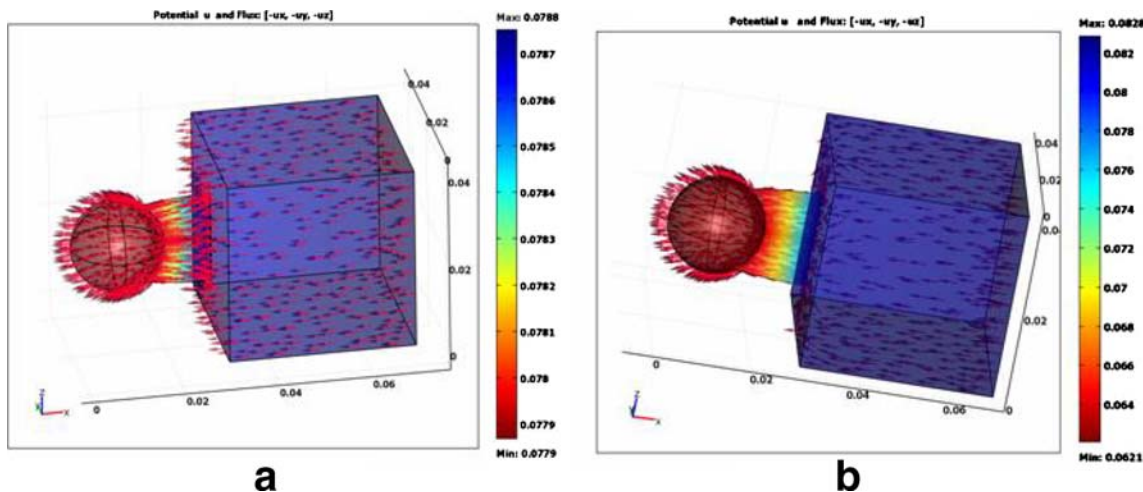

Fig. 10 Computed distribution of potential Φ (*colors*) and normalized potential flow $-\nabla\Phi$ (*arrows*) at time 1,000 s obtained with BC corresponding to an aqueous electrolyte (**a**) and an RTIL (**b**)
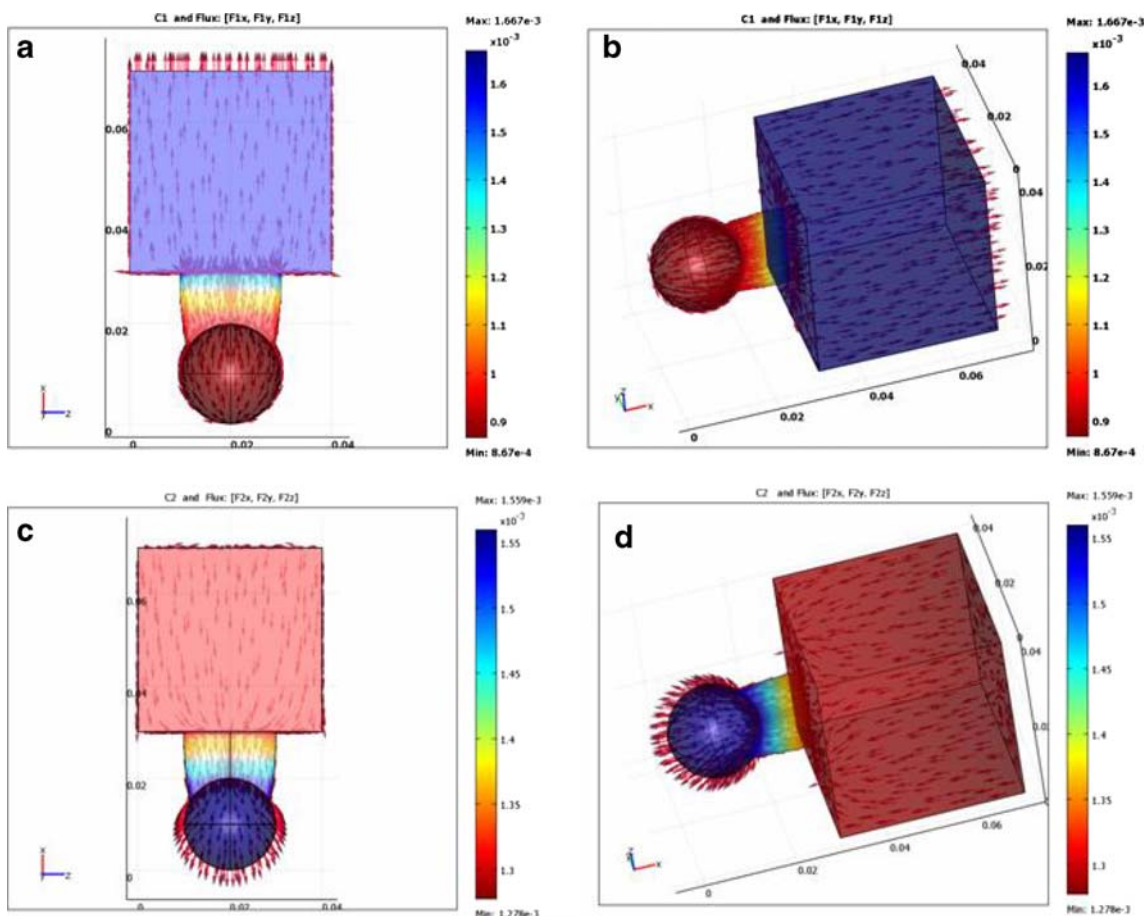
Fig. 11 Computed distributions of Cl^- (C_1, plots **a** and **b**) and Cu^+ (C_2, plots **c** and **d**) concentrations (*colors*) and respective normalized flows (*arrows*) at time 657 s obtained with BC corresponding to an RTIL
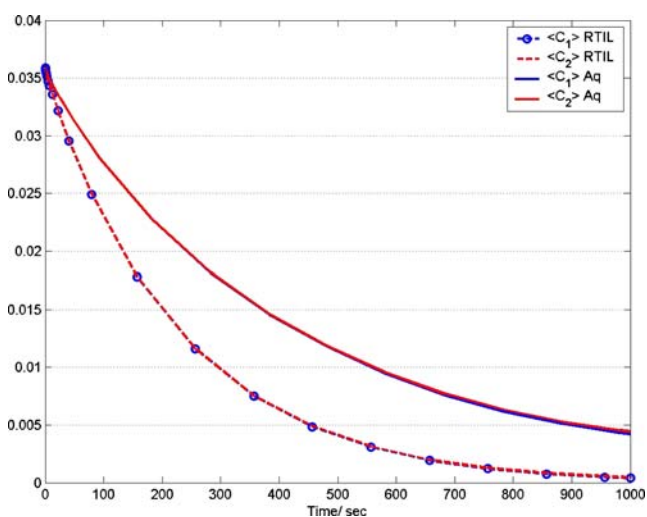

Fig. 12 Computed time dependence of the average concentrations of Cl^- (C_1) and Cu^+ (C_2) in the pore obtained with BC corresponding to an aqueous electrolyte and an RTIL

thus be taken to correspond to the electrical potential reference within our system, thus setting the IC $\Phi=0$ at this boundary. This choice does not impact the anodic kinetics because—as detailed in "Anodic BCs in RTIL"—the anodic current density is defined as homogeneous and corresponding to the value applied in the galvanostatic
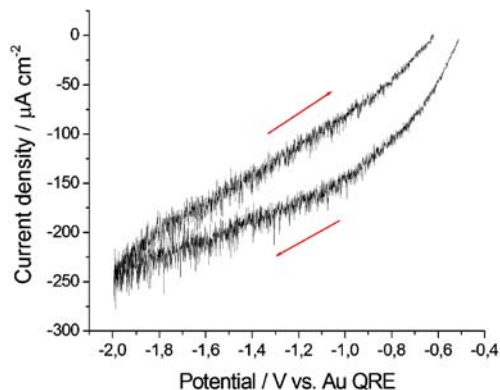

Fig. 13 Cyclic voltammetry of a fragment of the investigated object in contact with RTIL. Scan rate=1 mV s^{-1}
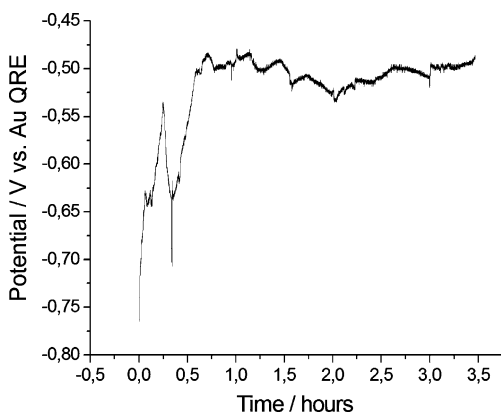
Fig. 14 Potential recorded during galvanostatic treatment at −100 μA cm^{-2} of the investigated object

experiments of interest. For numerical convergence reasons, on the cathodic boundary, such IC is chosen so that the initial current density vanishes.

Results of the numerical simulations

The differences in BCs implied by the use of the two types of electrolytes are most clearly highlighted by plotting the space distributions of the electrical potential Φ and its flux, $-\nabla\Phi$, of course directly proportional to the cathodic current

density. Since as $t \to \infty$, $C_1(x,y,z)=C_2(x,y,z)=\nabla\Phi(x,y,z)=0$, every nontrivial plot of the potential distribution corresponds to a given time of a transient. In Fig. 10, we show the distributions of Φ and $-\nabla\Phi$ (arrows) for the model constants listed below, at time 1,000 s. The water decomposition reaction gives rise to a cathodic current flow through the planar boundary at the right-hand side, corresponding to the outer surface of the bronze piece to be treated, and attending localization of the electric field.

In correspondence, concentration transients can be computed that describe the extraction of Cl$^-$ (C_1) from the pore into the outer electrolyte and deposition of Cu (C_2) at the inner pore surface. Representative concentration plots for C_1 (Cl$^-$) and C_2 (Cu$^+$), at time 657 s, are shown in Fig. 11; in these figures, we also show, by arrows, the fluxes of C_1 and C_2, denoting Cl$^-$ flow through the anodic border and Cu deposition at the bronze surface.

The power of using a RTIL with respect to an aqueous solution can be best appreciated by plotting the time dependence of the average concentration within the pore (i.e., actual pit and crack connecting it to the external electrolyte: blue boundaries in Fig. 9) that is obtained in correspondence of the respective cathodic BCs (Fig. 12). Notably shorter computed extraction time constants can indeed be assessed if the RTIL-BCs are employed: C_1, aqueous solution 388±6 s; C_2, aqueous solution 393±6 s; C_1, RTIL 277±4 s; C_2, RTIL 228±5 s.

Fig. 15 X-ray diffractograms of the investigated object before and after cathodic galvanostatic treatment at −100 μA cm^{-2} for 3.5 h (see Fig. 14)
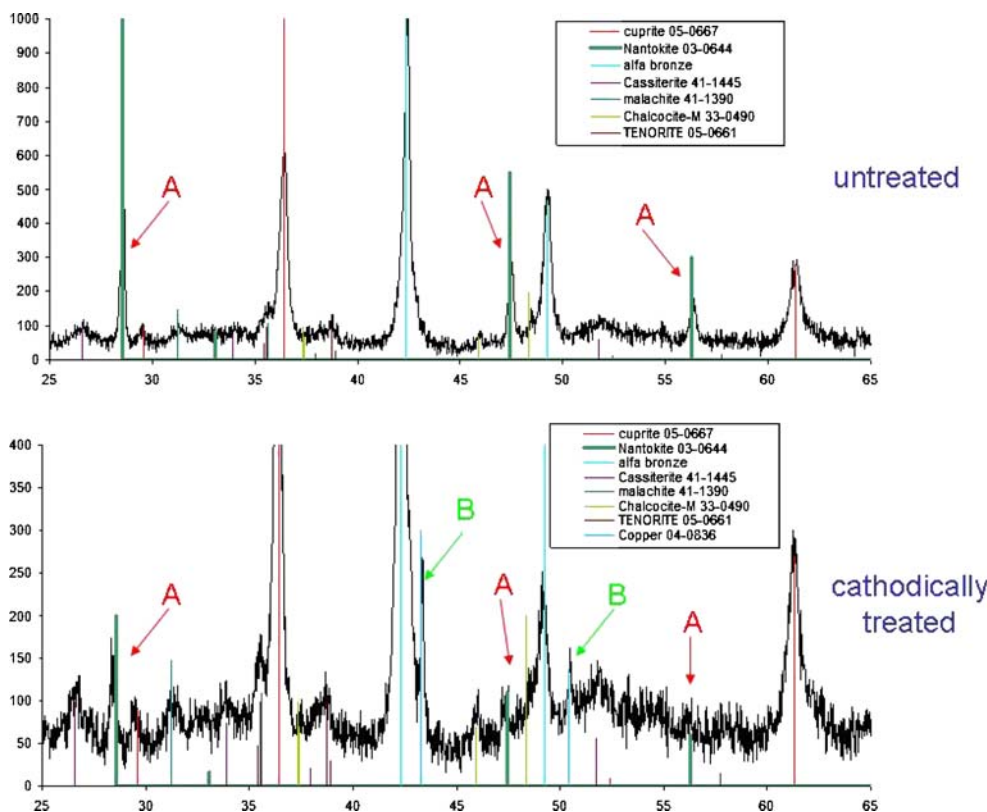
Electrochemical treatment and structural analysis of the cathodically treated object

Electrochemical treatment

Two essentially identical small pieces of the object were cut in such a way that approximately 0.5×0.5 cm^2 of patina could be exposed to EMI-TFSI. Since the electrochemical treatment is an irreversible one, one piece was used for exploratory CV work and the other one for the actual galvanostatic treatment. The CV shown in Fig. 13 is recorded in the potential range where the only active electrochemical reactions correspond to the reduction of patina components. Is it, of course, not an easy task to interpret the polarization curve in terms of reaction mechanisms because a host of different and irreversible processes are going on as a function of potential and polarization time. Nevertheless, it is possible to notice (1) a hysteresis, related to the irreversibility of the process; (2) a reduction of the current density in the return scan, corresponding to the consumption of some reducible material; and (3) a denobling of the corrosion potential that might be related to the activation of the metallic surface and the injection of chlorides into the initially neat RTIL.

For the reasons given in Section 3.2, the actual cathodic treatment has been carried out galvanostatically at -100 µA cm^{-2}, the time-dependent potential is reported in Fig. 14. The potential is initially at a level approximately corresponding to that found in Fig. 13, then settles down to a higher one. The fact that the potential does not decrease to values typical of RTIL cathodic decomposition witnesses that reduction of some patina component or other corrosion products continues during the whole experiment. The fact that the item we treated is a unique archeological artifact—with a peculiar patina that cannot be reproduced under controlled conditions—as well as the intrinsic irreversibility of the process, of necessity do not allow us to run replicated experiments or to extract more detailed information from the electrochemical measurements that are essentially a phenomenological time record of the process parameters. More information is, of course, derived from structural analyses of the treated object.

Structural analysis of the electrochemically treated object

In Fig. 15, we report the X-ray diffractograms corresponding to the investigated object before and after the cathodic galvanostatic treatment whose electrochemical conditions are shown in Fig. 14. The chief effects detected by XRD are (1) a notable reduction of the amount of nantokite (peaks A in Fig. 15)—corresponding to the removal of Cl$^-$ and Cu$^+$— and (2) the formation of metallic Cu (peaks B in Fig. 15). Since nantokite is contained in subsurface pits, as discussed

in Section 3.1, this result confirms that the aim of the treatment has been achieved.

Conclusions

In this paper, we report on galvanostatic cathodic chloride removal from a late bronze-age artifact found in the Roca site (Italy). The presence of Cu(I) chlorides, essentially in the form nantokite contained in subsurface pits, is correlated with bronze disease and attending severe, progressive damaging of historical artifacts exposed to marine environments. In this work, we propose the use of the RTIL EMI-TFSI as an electrolyte for electrochemical treatment, allowing the penetration of the cathodic conditions into the pits. This paper contains a detailed description of the patina, corrosion mode, and metallography of the as-found object—based on OM, SEM, and XRD—and an XRD investigation after treatment, proving notable reduction of nantokite content—corresponding to Cl$^-$ extraction— and formation of metallic Cu. Electrochemical data document the progress of the cathodic treatment. Numerical computations give theoretical support to the choice of RTIL as the medium for treatment and allow appreciating its advantages with respect to the traditional—though inefficient—aqueous solutions.

References

1. Lechtman H (1988) In: Maddin R (ed) The beginning of the use of the metals and alloys. MIT, Cambridge, pp 344–378
2. Giardino C (1998) I metalli nel mondo antico. Bari (I), Laterza, pp 151–157
3. Bozzini B, Giovannelli G, Pagliara C, Guglielmino R, Maggiulli G (2003) Ceremonial gold artefacts of the late bronze age from the deposition site of Roca: a metallurgical investigation. Proceedings of the "Archaeometallurgy in Europe", International Conference, Milan, Italy, September 24–26, p 267
4. Pagliara C (2001) Roca. Bibliografia Topografica Colonizzazione Greca Italia XVI:197–229. Roma-Pisa. I
5. Maggiulli G, Rivista di Scienze Preistoriche, LIX (2009) in press.
6. Organ RM (1963) Stud Conserv 8:1
7. MacLeod ID (1981) ICCM Bull VII(1):16
8. Robbiola L, Blengino J-M, Fiaud C (1998) Corros Sci 40:2083
9. Lucy VF (1972) Br Corros J 7:36
10. Mankowski G, Duthil JP, Giusti A (1997) Corros Sci 39:27
11. Pourbaix M (1976) J Electrochem Soc 123:25c
12. Giangrande C (1987) In: Black J (ed) Recent advances in the conservation and analysis of artifacts. Summer School, London, p 135
13. Veleva L, Quintana P, Ramanauskas R, Pomes R, Maldonado L (1996) Electrochim Acta 41:1641
14. Tennent NH, Antonio KM ICOM Committee for Conservation 6th Triennial Meeting, Ottawa 81/23/3-1
15. Payer JH, Ball G, Rickett BI, Kim HS (1995) Mater Sci Eng A 198:91
16. Fink C, Eldridge CH (1923) Efficient method for restoration of antique bronzes badly corroded or crusted over. Unpublished typescript, Walters Art Gallery, Baltimore, Maryland

17. Bazzoni B, Bazzoni A, Pedeferri P, Lazzari L, Bertolini L (1996) Corrosion/96, NACE, paper 312

18. Bertolini L, Bolzoni F, Pastore T, Pedeferri P (1998) Corrosion 98/NACE, paper 639

19. Bertolini L, Bolzoni F, Lazzari L, Pastore T, Pedeferri P (1998) J Appl Electrochem 28:1321

20. Plenderleith HJ (1995) The conservation of antiquities and works of art. Oxford University Press, London

21. Walters Correspondence. Archives, Walters Art Gallery Conservation Laboratory, Baltimore, Maryland

22. Weisser T (1975) The de-alloying of copper alloys. In: Conservation in archaeology and the applied arts. International Institute for Conservation of Historic and Artistic Works, London, pp 207–214

23. Madsen HB (1967) Stud Conserv 12:163

24. Tennent NH (1997) Conservation science: a view from four perspectives. In: Bradley S (ed) The interface between science and conservation. British Museum Occasional Paper No. 126, London

25. Katiforis N, Papadimitriou G (1996) Surf Coat Technol 78:185

26. PowderCell 2.3—Pulverdiffraktogramme aus Einkristalldaten und Anpassung experimenteller Beugungsaufnahmen. Available at http://www.bam.de/de/service/publikationen/powder_cell.htm

27. Giovannelli G, Bozzini B, Natali S (2005) Archaeometry 47:817

28. Endres F, MacFarlane D, Abbott A (eds) (2008) Electrodeposition from ionic liquids. Wiley-VCH, Weinheim

29. COMSOL Multiphysics, v.3.5 (2008) Modeling guide

30. Sidot E, Kahn-Harari A, Cesari E, Robiola L (2005) Mater Sci Eng A 393:147

31. Chase WT (1994) Chinese bronzes: casting, finishing, patination, and corrosion. In: Scott DA, Podany J, Consadine BB (eds) Ancient and historic metals: conservation and scientific research. J. Paul Getty Museum and the Getty Conservation Institute, Marina del Rey, pp 85–118

32. Acharya NN (2001) J Mater Sci 36:4779

33. McCann LI, Trentelman K, Possley T, Golding B (1999) J Raman Spectrosc 30:121

34. McNeil MB, Little BJ (1999) JAIC 38:186

35. Frost RL, Williams PA, Martens W, Kloprogge JT (2002) J Raman Spectrosc 33:752

36. Gavrilenko ON, Pashkova EV, Belous AG (2007) Russ J Inorg Chem 52:1835

37. Bertolini L, Elsener B, Pedeferri P, Polder R (2004) Corrosion of steel in concrete. Wiley-VCH, Weinheim, pp 364–369

38. Koryta J, Dvorak J, Kavan LJ (1993) Principles of electrochemistry, 2nd edn. Wiley, Chichester

39. Hine F (1985) Electrode processes and electrochemical engineering. Plenum, New York

40. Soares DM, Wasle S, Weil KG, Doblhofer K (2002) J Electroanal Chem 532:353

41. Despic AR (1983) In: Conway BE, Bockris JOM, Yaeger EB, Khan SUM, White RE (eds) Comprehensive treatise of electrochemistry, vol 7. Plenum, New York

42. Bozzini B, D'Urzo L, Gianoncelli A, Kaulich B, Prasciolu M, Sgura I, Tondo E, Kiskinova M (2009) An in situ synchrotron-based soft X-ray microscopy investigation of Ni electrodeposition in a thin-layer cell. J Phys Chem C (in press)